Sādhanā (2022) 47:203
https://doi.org/10.1007/s12046-022-01977-1

Investigation effect of resistance spot welding parameters on dissimilar DP1000HF/CP800 steel joints

MELIH KEKIK[1,2], FATIH ÖZEN[3,*], VOLKAN ONAR[4] and SALIM ASLANLAR[5]

[1] R&D Department, AK Pres Automotive Manufacturing Co, 2th Organized Industrial Zone, 2nd Road, 54300 Hendek, Sakarya, Turkey
[2] R&D Department, AK Automotive Manufacturing Co, Cesta Marezganskega upora 2, 6000 Koper, Slovenia
[3] Department of Machinery and Metal Technologies, Beşiri Organized Industrial Zone Vocational College, Batman University, 72000 Batman, Turkey
[4] Department of Mechanical and Manufacturing Engineering, Faculty of Technology, Pamukkale University, 20260 Denizli, Turkey
[5] Department of Metallurgical and Materials Engineering, Faculty of Technology, Sakarya University of Applied Sciences, 54187 Sakarya, Turkey
e-mail: melihkekik@gmail.com; fatih.ozen@batman.edu.tr; vonar@pau.edu.tr; aslanlar@sakarya.edu.tr

MS received 16 February 2022; revised 16 August 2022; accepted 17 August 2022

Abstract. Recently, advanced high strength steels (AHSS) have gained importance especially in automobile industry due to excellent tensile and elongation properties. Dual phase and complex steels are among prominent members of the AHSS family. DP steels contains martensite within the ferrite matrix while the CP steels contains bainite, retained austenite, martensite and ferrite. The tensile strength of these steels can reach up to 1200 MPa. Also, new grades of the DP steels offer high formability with high tensile strength. In this work, resistance spot weldability of dissimilar CP800 and high formability grade of DP1000HF steel joint were investigated. Tensile-shear tests, weld nugget diameters and electrode indentation depths were evaluated with microstructural examinations. A weld lobe was determined in the light of obtained findings and standards. According to the results, SCHAZ of the DP1000HF is the weakest region of the joint affecting the tensile-shear strength. Maximum tensile-shear strength was 26380 N at 25 cycle welding time and 9.44 kA welding current where diameter of the weld nugget was measured as 9780 µm. Interfacial fracture separation mode was generally obtained below weld nugget diameter of 7500 µm. CP800 exhibited less electrode indentation depth compared to DP1000HF. The difference in electrode indentation depths between CP800 and DP1000HF was increased by raising the heat input.

Keywords. AHSS; dual phase steels; complex phase steels; high formable dual phase; resistance spot welding.

1. Introduction

Due to carbon emissions, energy shortage, limited fossil fuels and increasing fuel prices, automotive manufacturers have sought new and inexpensive materials for low weight vehicles [1]. It also should be a material to reduce vehicle weight without compromising safety [2]. To address these demands, the steel manufacturers have begun to develop new generation steels. Firstly, high strength low alloy steels were developed (HSLA). However, their tensile strengths were limited [3]. Later, with significant progress in the steels, advanced high strength steels (AHSS) have been developed [4]. Versatile design needs on the vehicle have led to developing of new type AHSS including dual phase (DP), complex phase (CP), transformation induced plasticity (TRIP), twinning induced plasticity (TWIP) steels, etc. [5].

Dual phase (DP) steels contains only martensite in a ferrite matrix [6]. These steels are designed as a low-cost solution to provide a high-strength-weight ratio [7]. For this reason, these steels have found vast amount of application area in the automotive body parts such as body panels and bumpers [8]. While ranges for tensile strengths of DP steels are between 500 and1500 MPa, the elongations are between 7 and30% [9, 10]. However, obtaining high strength with simultaneously high ductility is difficult to achieve [11, 12]. By designing the properties including constituent microstructure, volume fraction of the phases and morphology, DP steels with high strength with good formability grades can be produced [13–16].

The forming problems encountered during production, the non-coexistence of high strength and high elongation,

---

*For correspondence

and the desire to absorb more impact energy have led to the development of Complex Phase (CP) steels [17, 18]. The CP steels contains a good combination of ferrite, bainite, martensite and retained austenite leading to high yield strength and better elongation [19, 20] Thereby, impact resistance and ductility have been improved without loss tensile strength [21, 22]. The problems belong to forming process was also improved. Better edge flanging, high resistance to the edge cracking and improved bending have been obtained [23]. These steels have found application area on vehicles as door impact bars, sills, seat rails, torsion beams and chassis components [20, 24].

Although microstructure of the AHSS was designed to meet engineering demands, less care about their weldability was taken into consideration, especially welding with resistance spot welding (RSW). RSW is the most employed welding method in automotive manufacturing [25]. An average vehicle can contain between 2000 and 5000 spot welds [26, 27]. It affects the local properties of the tightly engineered microstructure and then, the joint performance. For this reason, investigating the RSW method is of high importance.

In literature, studies about weldability of dissimilar CP and DP joints have solely been coincided for laser welding and stir spot welding techniques [11, 24]. The DP steels with high formability grades have not been studied in literature as well. Furthermore, weldability of CP steels have not been widely studied. In this study, resistance spot weldability of the dissimilar DP1000HF (high formable grade) with CP800 steel joint was investigated. Tensile-shear tests, weld nugget diameter and electrode indentation depths were evaluated in terms of welding currents and welding times. Microstructural investigations were made with SEM, SEM/EBSD and optical microscope. Microhardness from the weld section was also taken to evaluate the microstructure. In the light of the results, a weld lobe curve was created.

2. Materials and method

Cold rolled CP800 and DP1000HF steels with 1.4 mm thickness were used in experiments. The chemical composition and mechanical properties of both steels are presented in Table 1 and Table 2, respectively. The CeV is the calculated carbon equivalence of both steels.

The steel sheets were sliced to 30 × 100 mm for tensile-shear tests. The specimens were ultrasonically cleaned for 30 min and chemically cleaned with acetone to remove oil and dirt. A resistance spot welding machine having 120 kVA capacity with pneumatically controlled jaws was used for the RSW. The welding currents and welding times were adjusted with electronic control interface. The welding parameters were constantly measured with Dengenshia WS-100 welding apmeremeter. The tensile-shear test specimens were welded with 30-mm overlapped position. A welding fixture was used to maintain the positional precisioning. The welded position and its dimensions for the tensile-shear test specimen is presented in Figure 1. Cu-Cr electrodes with 6 mm contact surface diameter were employed. The electrodes were cooled with 6 l/min constant water flow. Electrode application force was adjusted to 4 kN and regularly measured. Clamping time and holding time were adjusted to 25 cycle (1 cycle equals to 0.02 s).

The welding currents and welding parameters used in experiments are illustrated in Table 3. Each welding parameters repeated three times and average values were utilized for the charts. The welded specimens were cut from the cross section of the weld nugget. Then, standard metallographic processes were implemented for macro and microstructural investigations. The microstructure was etched using 5% Nital for 7 s. Microstructures were examined using Nikon Eclipse L150A optical microscope. FEI Quanta 200 FEG SEM/EBSD device was also used for microstructural investigations. Macrostructural measurements such as weld nugget diameter and electrode indentation depths were performed with Nikon SMZ745T stereo microscope. The measurement of grain size and phase distributions were measured via SEM images with Clemex Lite image analysis software according to ASTM E112 standard. EBSD technique was also used for phase distribution and grain size analysis. Figure 2 shows the hardness measurement line from the cross section of the RSW. Hardness measurements was carried out with Vickers Wilson Hardness tester under 0.098 N load for 10 s. There was a 0.25 mm gap between each hardness points. Tensile-shear tests was executed with SHIMADZU AGS-50kN universal testing machine. Tensile-shear tests were performed with 10 mm/min crosshead speed.

3. Results and discussion

3.1 *Microstructural observations*

3.1.a *Base metals*. SEM devices have an important role in imaging of the microstructure. Figure 3a shows the SEM

Table 1. Chemical composition of CP800 and DP1000HF steel. (wt.-%)

Steel	C	Si	Mn	Cu	Al	S	Cr	Ti	Ni	Nb	Mo	V	B	Fe	CeV
CP800	0.133	0.19	1.49	0.01	0.039	0.001	0.04	–	0.05	–	0.02	0.01	–	Rest	0.40
DP1000HF	0.112	0.93	2.7	–	0.046	–	–	0.002	–	0.002	–	–	0.0002	Rest	0.56

Table 2. Mechanical properties of the CP800 and DP1000HF steel.

Steel	Tensile strength (MPa)	Yield strength (MPa)	Elongation (%)
CP800	839	642	12.5
DP1000HF	1042	728	14.2

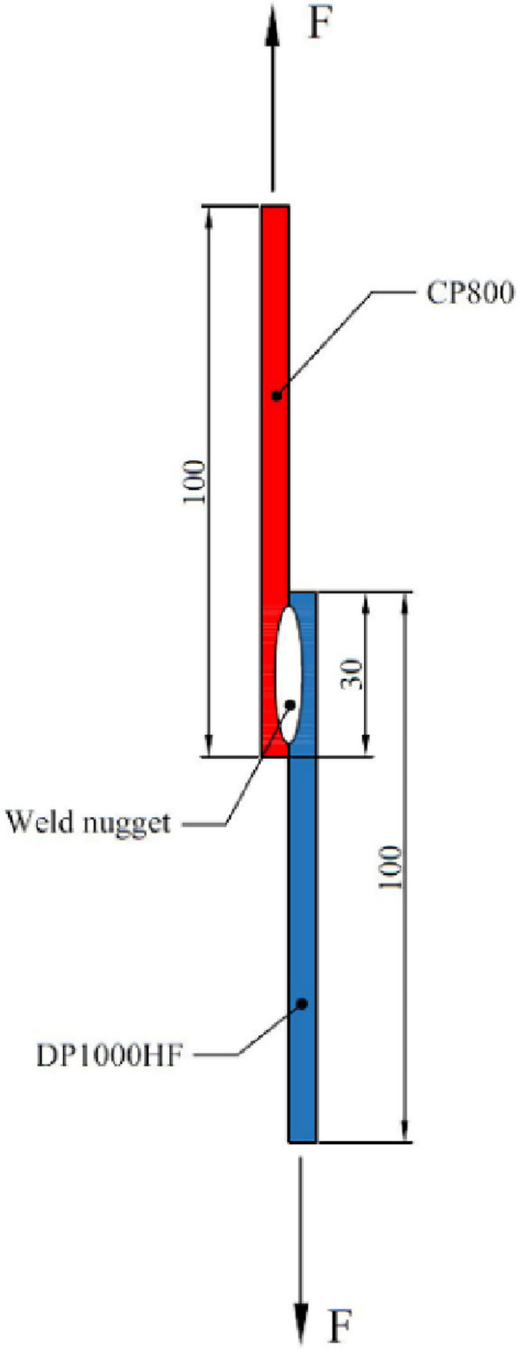

Figure 1. Dimensional details of the RSW applied tensile-shear test specimen.

Table 3. Welding parameters used in experiments.

	Welding times (cycle)					
	5	10	15	20	25	30
Welding currents (kA)						
5.8	–	–	14	22	28	33
7.1	–	7	15	23	29	34
8.2	1	8	16	24	30	35
9.6	2	9	17	25	31	36
11.5	3	10	18	26	32	37
13.4	4	11	19	27	–	–
14.6	5	12	20	-	–	–
15.4	6	13	21	-	–	–

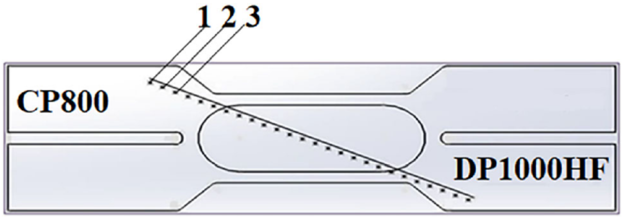

Figure 2. Hardness measurement sequence of RSW applied specimen.

image obtained from the base metal (BM) of CP800 steel with the magnification of 5 kX. Bainite, retained austenite, martensite and ferrite islands were observed in the microstructure of CP steel. Although the retained austenite was not clearly obvious in SEM microstructure of CP800, its presence in BM was also described in EBSD analyses (Figure 8d). Histogram graph of grain size distributions from base metal of CP800 is shown in Figure 3b. Ranges for grain sizes are between 2 and 11 µm. Average hardness of BM was measured as 332 Hv.

Figure 4a shows the SEM image of DP1000 steel with enhanced formability grade (DP1000HF), obtained with the magnification of 5 kX. It consists of ferrite and martensite. Martensites were formed at the edges of ferrite grains. Figure 4b illustrates histogram graph of grain size distributions from base metal of DP1000. Based on at least 90% confidence level, the range for size of the ferrite is between 3 and 12 µm, while the range for size of the martensites are

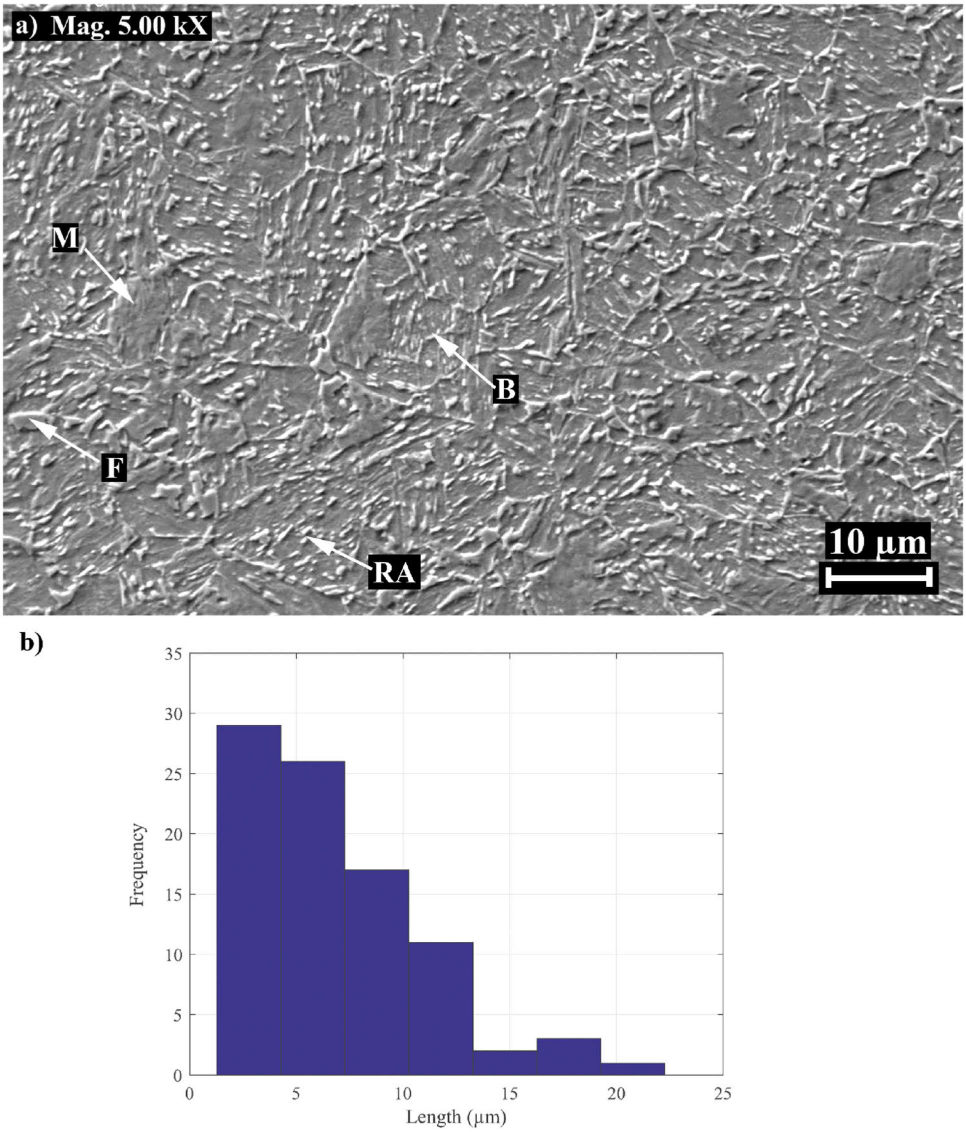

Figure 3. **a**) SEM image of CP800 steel from BM and **b**) Histogram graph for grain distribution.

between 1 and 4 µm. The average microhardness was measured as 340 Hv.

It is find out that traditional dual phase steels that have 1000 MPa tensile strength (DP1000) have various size and distribution of martensite and ferrite in the microstructure [28, 29]. DP1000HF has much finer martensite size at the edges of polygonal ferrites than conventional DP1000. The size of the ferrite is also finer than traditional DP1000 steels. The ferrite ratio in the microstructure is also higher than conventional DP1000 steel. Therefore, the formability of DP1000HF steel has increased.

Quantitative phase analysis results from BM of CP800 and DP1000HF is presented in Table 4. CP800 was consisted of 44.3% ferrite, 44.5% bainite, 9.8% martensite and 1.4% retained austenite while DP1000HF was composed of 47.1% martensite and 52.9% ferrite.

3.1b *Heat affected zones*. The microstructural characteristic of the joint is an important factor that determines the joint strength, rupture behavior and elongation properties. The HAZ region is also a significant region that affected by the heat input applied during welding. It can lead to the microstructural change and directly affects the type of fracture. If HAZ region of DP and CP steels is examined, both steels exhibited similar microstructural divisions. Four different regions were formed in HAZ of the both steels. These are: i) sub-critical heat affected zone (SCHAZ), ii) inter-critical heat affected zone (ICHAZ), iii) fine grained heat affected zone (FGHAZ) and iv) coarse grained heat affected zone (CGHAZ). These regions also coincided in the literature while welding of ferritic-martensitic and bainitic steels [30, 31].

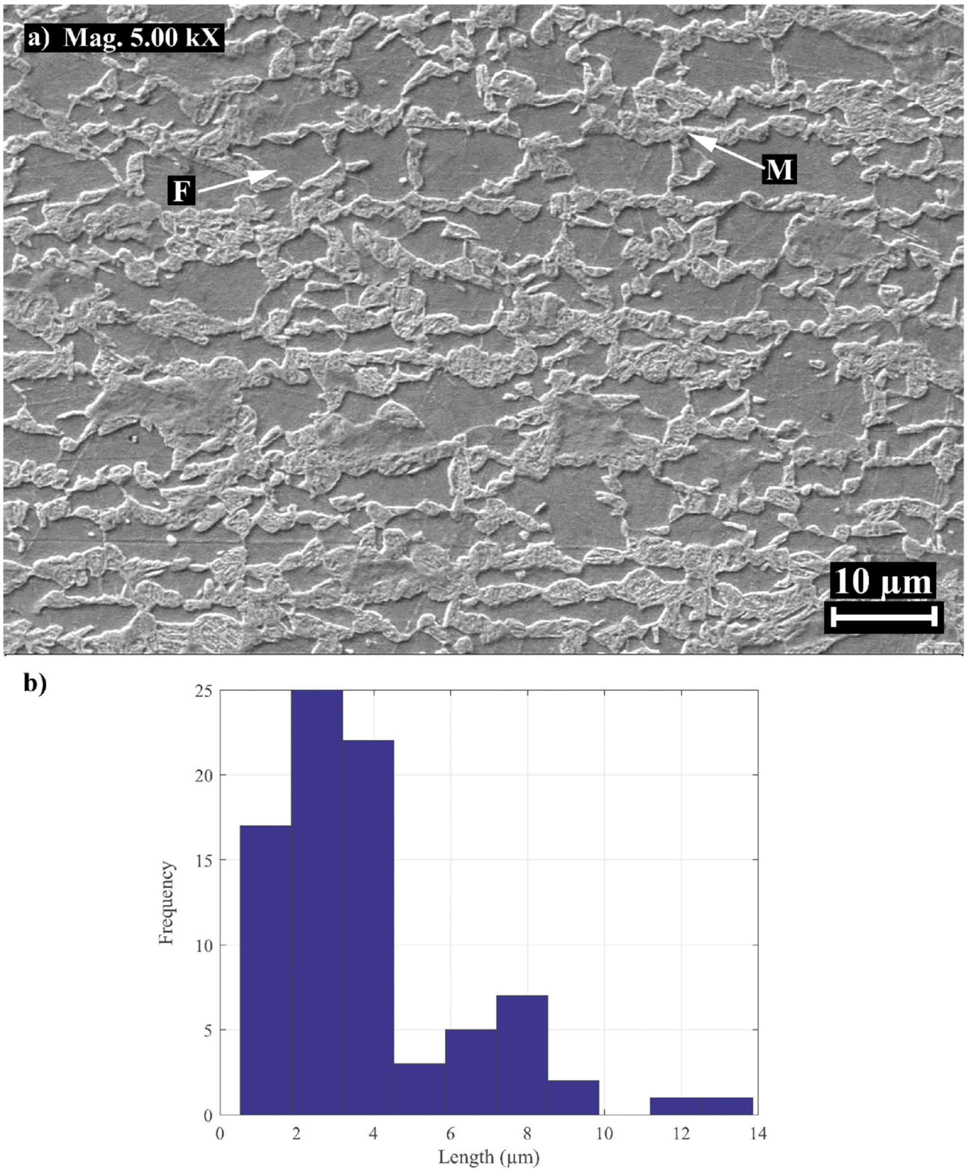

Figure 4. **a**) SEM image of the DP1000HF steel from BM and **b**) Histogram graph for grain distribution.

Table 4. Quantitative phase distribution of the DP1000HF and CP800 steel.

	Phase fraction (vol.-%)			
	Retained Austenite	Bainite	Martensite	Ferrite
CP800	1.4	44.5	9.8	44.3
DP1000HF	–	–	47.1	52.9

The SCHAZ is the region below the A_{c1} temperature, partially exposed to heat between 600 and720°C for a brief time. ICHAZ is the region between A_{c1} and A_{c3} critical temperatures. FGHAZ and CGHAZ formed during cooling from austenite. The cooling gradient which affected the size of the grains while cooling formed the FGHAZ and CGHAZ.

Microstructural images from HAZ of DP1000HF are shown in figures 5a-e. Particles in the microstructure appearing as white represent ferrite and black ones represent the martensite. The result of microhardness taken along the cross section is shown in Figure 6. In the SCHAZ region, the hardness decreased with the temperature reaching below the A_{C1} critical temperature (500-723°C). As seen in Figure 5e, the pre-existing martensites were tempered because of sub-A_{C1} temperature at SCHAZ. The tempered martensite caused a significant decrease in hardness at SCHAZ. The tempered martensite transformed into cementite by dispersing in the ferrite grains along prior

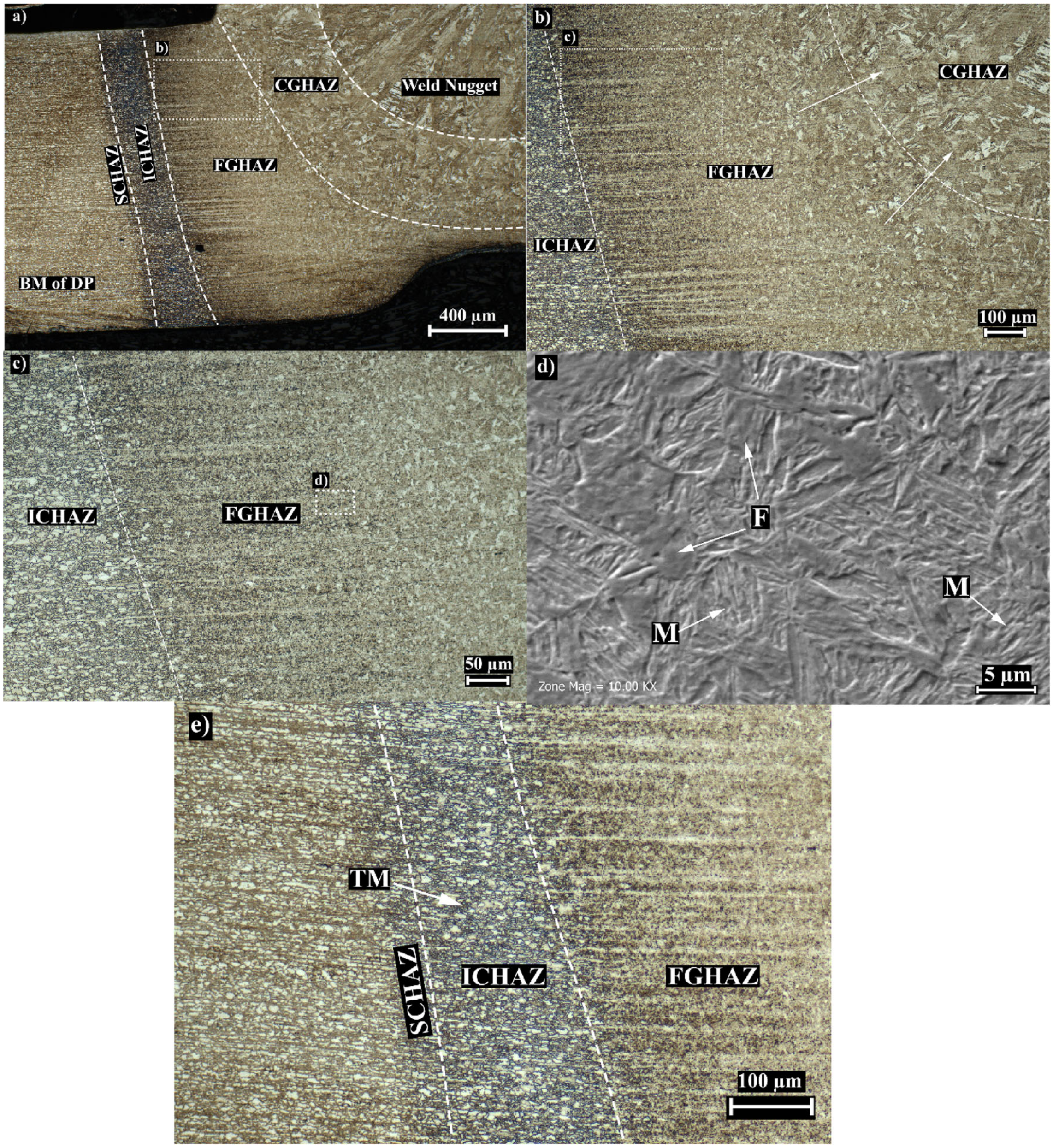

Figure 5. HAZ of the DP1000HF with **a**) 50x, **b**) 100x, **c**) 200x, **d**) 10 kx from HAZ and **e**) 200x from SCHAZ/ICHAZ/FGHAZ interface.

existing lath locations [32]. The volume of the martensite is the most effective factor determining degree of softening [33]. Thereby, polygonal ferrite and randomly formed granular carbide (cementite), which are products of the tempered martensite, decreases hardness of the microstructure. Softening of SCHAZ in dual phase steels also mentioned in the literature. Wang *et al* [34] studied influence of heat input on the microstructure and properties of laser welded DP1000 butt joints. They find out that a significant decrease in hardness were observed in the SCHAZ. Martensite in SCHAZ was tempered and decomposed into polygonal ferrite and granular carbide. Thereby, hardness of the SCHAZ was significantly decreased. Chen *et al* [31] investigated resistance spot weldability of Q&P 1180 steel. Q&P steels are mainly composed of martensite and retained austenite. It was found that hardness of SCHAZ was substantially decreased due to tempering the martensite.

The degree of tempering in martensite depends on application time and temperature. The maximum tempering is yielded just before A_{C1} temperature (723°C) where the cementite is commenced to be transformed into austenite. Therefore, the hardness reduction reaches its highest point at this SCHAZ/ICHAZ interface. The softening increases as

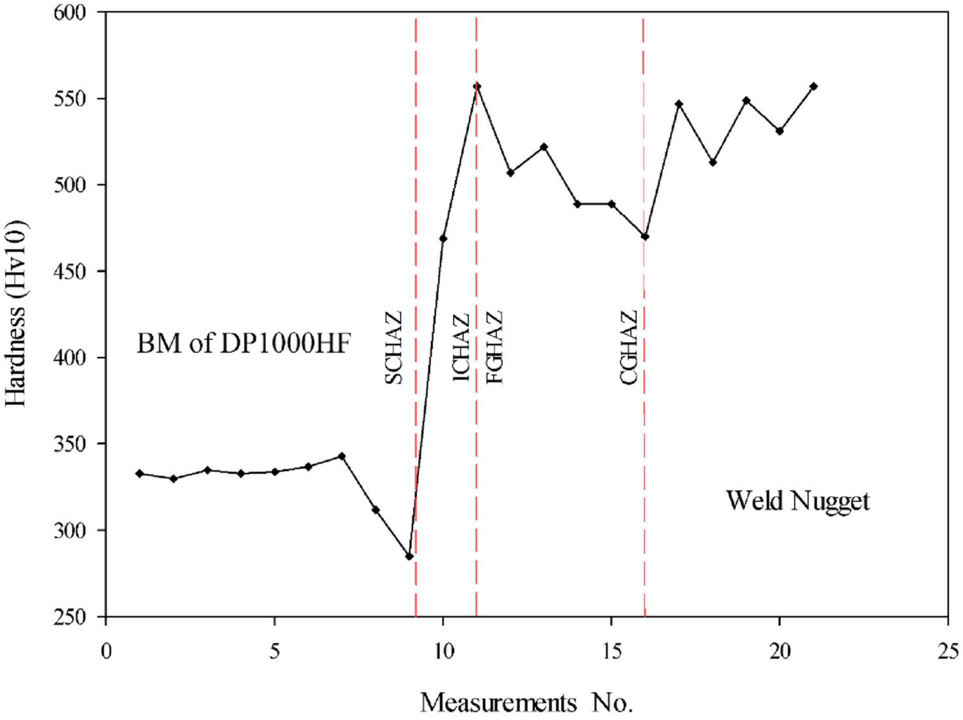

Figure 6. Hardness profile of DP1000HF side.

it approaches the A_{C1} temperature. It was reported that the softening behavior of the DP steels heavily influenced by welding heat input and material chemistry [35]. Moreover, the volume of the martensite at the BM of the DP steels influences the degree of the softening [33]. The degree of the softening could be optimized by controlling the heat input.

As seen from Figure 5c, Ferrite gradually transforms into austenite as it moves from the ICHAZ to the FGHAZ. Exceeding the A_{C3} critical temperature, which also describes the frontier between ICHAZ and FGHAZ, causes fully austenite transformation. With the rapid cooling of the austenite, the smallest grain size and the highest hardness point was obtained at FGHAZ [36, 37]. Since austenite was transformed into a martensitic microstructure with small grain size, the high hardness can be expected. The hardness at this point was measured as 554 Hv. The grain size was increased as move to CGHAZ/weld nugget interface. As approached to CGHAZ/weld nugget interface, coarsed martensite was obtained with slower cooling caused a decrease in hardness.

Microstructure images from HAZ of the CP800 steel is illustrated in Figures 7a-e with various magnifications. EBSD analysis of CP800 from BM to ICHAZ is presented in Figures 8a-d that illustrated inverse pole figure (IPF) map, image quality (IQ) map, IQ+IPF map, and phase distribution map, respectively. Hardness distribution from the BM of the CP800 to weld nugget zone is presented in Figure 9. Phase distributions was analyzed on the basis of cementite (Fe_3C), ferrite and austenite. The austenite represents retained austenite (RA) of CP800. Grains from BM to SCHAZ were elongated across the sheet section. These elongated grains are generally formed <111> and <101> directions. As move from BM to SCHAZ, some formations were observed on grains edges and the size of the grains were suddenly decreased. In this location, the microstructure was commenced to be influenced by welding temperature as seen in Figure 8a-c. The bainite and martensites was tempered and caused dispersion of the carbides leading to a dramatic decrease in the hardness. While hardness at ICHAZ/SCHAZ of the CP800 interface was 324 Hv, the hardness that of DP1000HF was 280 Hv. Since the martensite fraction in BM of DP1000HF is higher than BM of CP800, the DP1000HF exhibited softer microstructural behavior than CP800 at SCHAZ/ICHAZ interface.

By exceeding the A_{c1} temperature ($\sim$723°C), the carbides were transformed into austenite and the ferrite was gradually transformed to austenite by the end of the ICHAZ. This transformation was completed at the boundary of the FGHAZ/ICHAZ. At this stage, the transformation of the retained austenite to fully austenite is not expected. Upon entering the FGHAZ region, the unstable retained austenite was completely dissolved and lost its existence in the HAZ microstructure.

Beyond the FGHAZ/ICHAZ line, fully austenite transformed into bainite and martensite as seen in the Figure 7d. Formation of the bainite at HAZ of the CP800 was also addressed by some researchers [11, 30] Much smaller grain

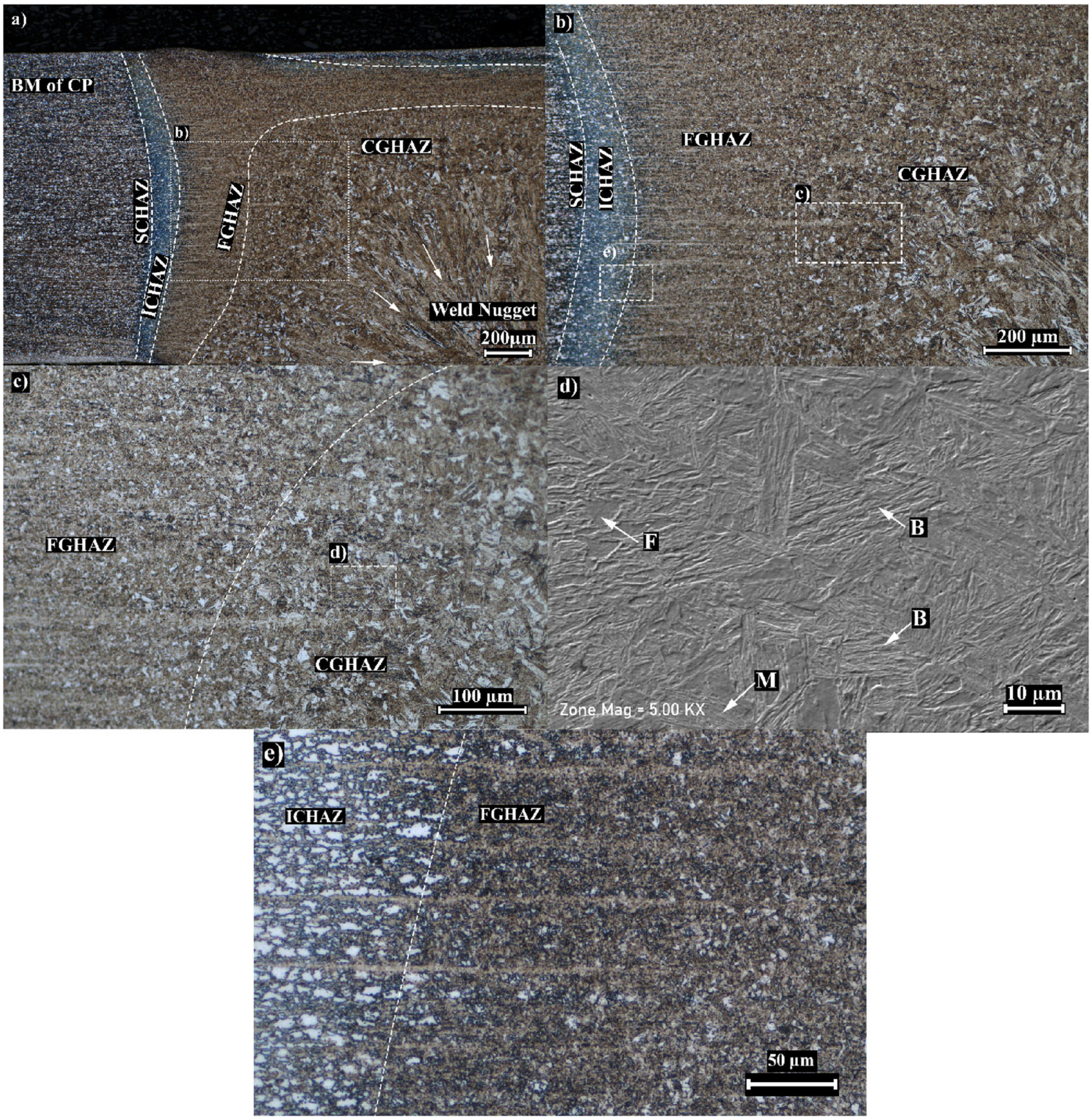

Figure 7. HAZ of the CP800 with **a**) 50x, **b**) 100x, **c**) 200x, **d**) 5000x from HAZ and **e**) 200x from ICHAZ/FGHAZ interface.

size was obtained in the FGHAZ region compared to DP1000HF steel. The heat input was increased as being close to melted fusion zone. Therefore, lowest heat input and quick dissipation of the heat to the sheet itself causes finer grains as seen in Figures 8b and c. Formation of fine granular bainitic and martensitic structure is the main reason for high hardness in FGHAZ/ICHAZ interface. The grain coarsening from FGHAZ to CGHAZ due to slow cooling rate was also similar to that of coincided into DP1000HF steel. The largest grains were observed at the CGHAZ/weld nugget interface due to heat input from the weld nugget. The hardness was relatively decreased due to grain coarsening. The hardness decreases proportionally to the grain size at FGHAZ and CGHAZ.

3.1.c *Weld Nugget*. Microstructure from the weld nugget of the RSW applied DP1000HF/CP800 steel is presented in Figure 10a-d. The weld nugget represents fully melted zone during RSW. The microstructure of the weld nugget is consisted of martensite and some ferrite islands. The martensite was consisted of needle-like martensite laths packs with various orientations. The martensites have different lath thicknesses and sizes. Since the last solidifying zone is the center of the weld nugget, the microstructure formed columnar and followed the cooling gradient. Average hardness was measured as 520±50 Hv. The hardness is consistent with martensitic structure. High divergence in hardness of weld nugget can be explained by various size and thickness of the martensite laths. Similar

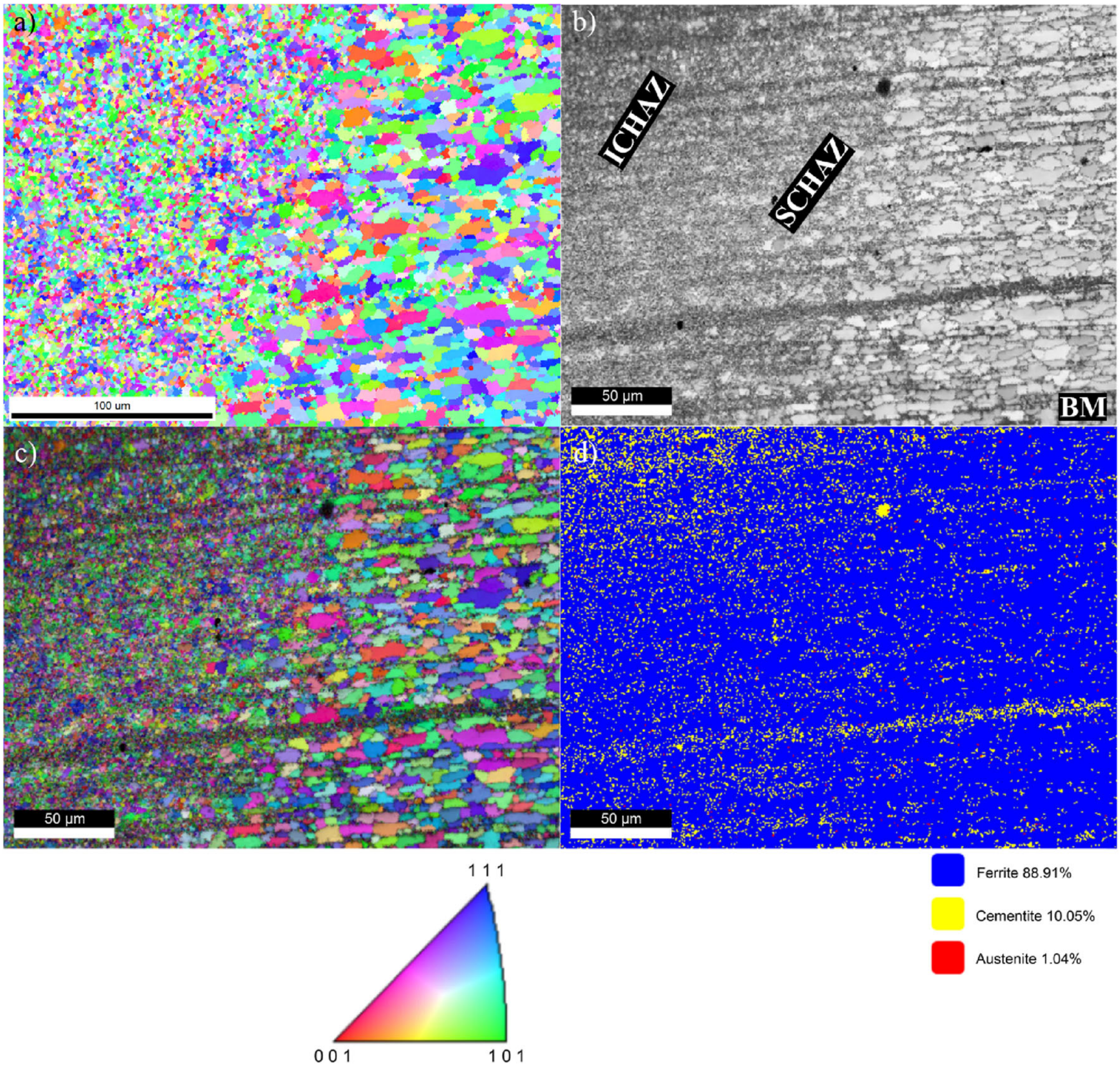

Figure 8. EBSD analysis from BM to ICHAZ region of CP800 steel: **a**) Inverse pole figure (IPF) map, **b**) Image quality (IQ) map, **c**) IQ+IPF map, and **d**) Phase distribution map.

results were also obtained in the literature as well. Kong *et al* [17] studied effect of various boron content on resistance spot weldability. They obtained a fully martensitic and ferritic microstructure in weld nugget and microstructure of weld nugget is not heavily influenced by boron content.

Morawiec *et al* [38] studied laser weldability of hot-rolled complex phase steel grades with single and dual laser spot beam technique. They discovered that the fusion zone contained a fully martensitic lath structure.

3.1.d *Fracture surface.* The characteristic of the fracture surface provides important clues in determining the degree of ductility or brittleness of the material. The way that surface rupture determines the characterization of the microstructure at the rupture location. Figures 11a-d show the SEM image from the rupture surface with different magnifications. It can be seen that the rupture first starts normal to the sheet surface and progresses along the outside of the HAZ. Since hardness of the SCHAZ is relatively softer than other regions, the rupture commenced from SCHAZ. The decreased hardness of SCHAZ behaves like a notch effect that envelops the HAZ. Therefore, the crack formed at the beginning of the rupture breaks through the SCHAZ.

The presence of high amounts of dimple were observed on the rupture surface. The dimples are a sign of ductile rupture. However, cleavage formations were also observed. The ruptures happened continuously on the DP1000HF side. The weakest location is SCHAZ of the DP1000HF as the amount of softening in the SCHAZ zone is more severe

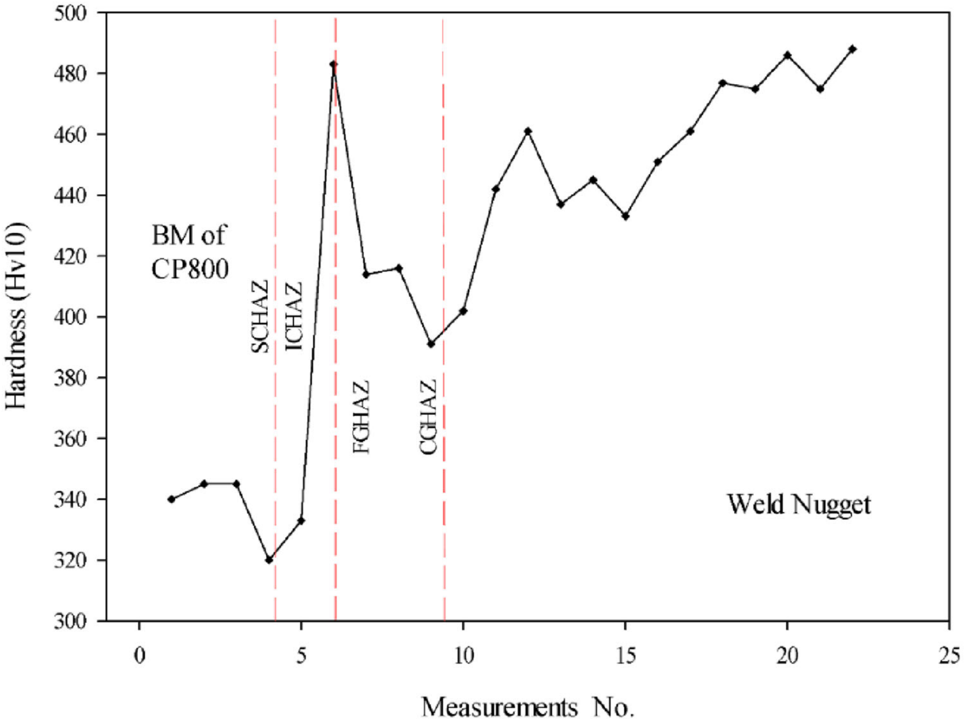

Figure 9. Hardness profile of the CP800 side.

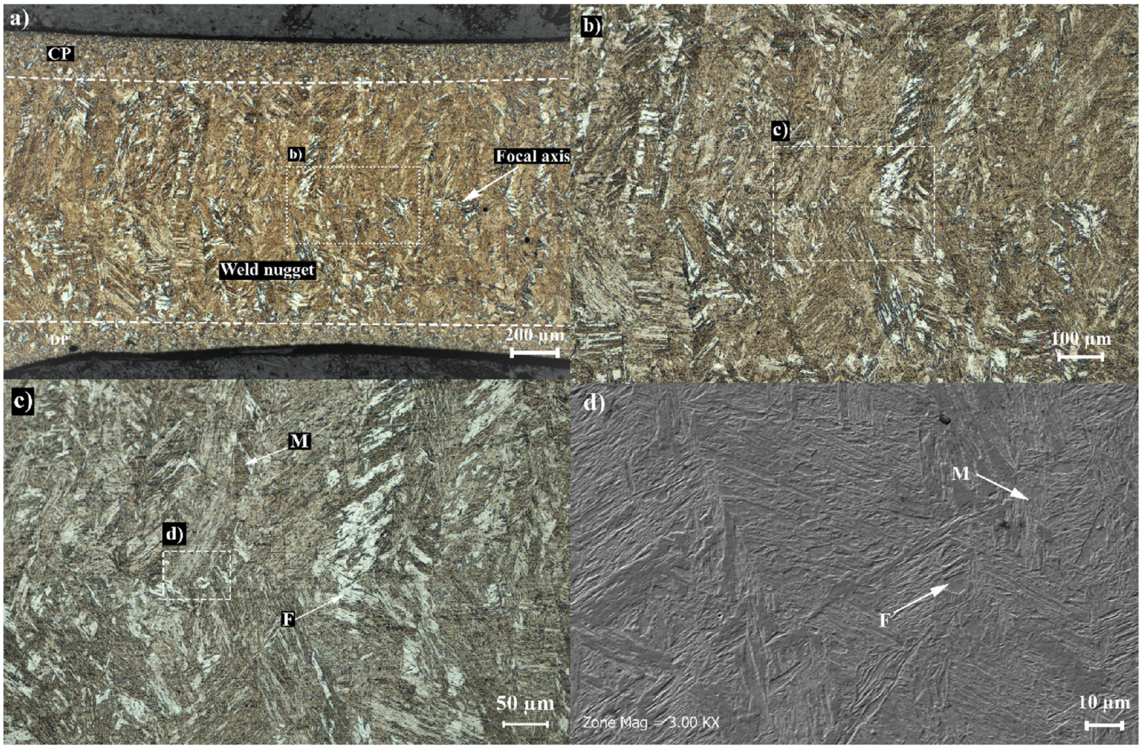

Figure 10. Microstructure from the weld nugget of CP800/DP1000HF with the magnifications of **a**) 50x, **b**) 100x, **c**) 200x and **d**) 3000 x.

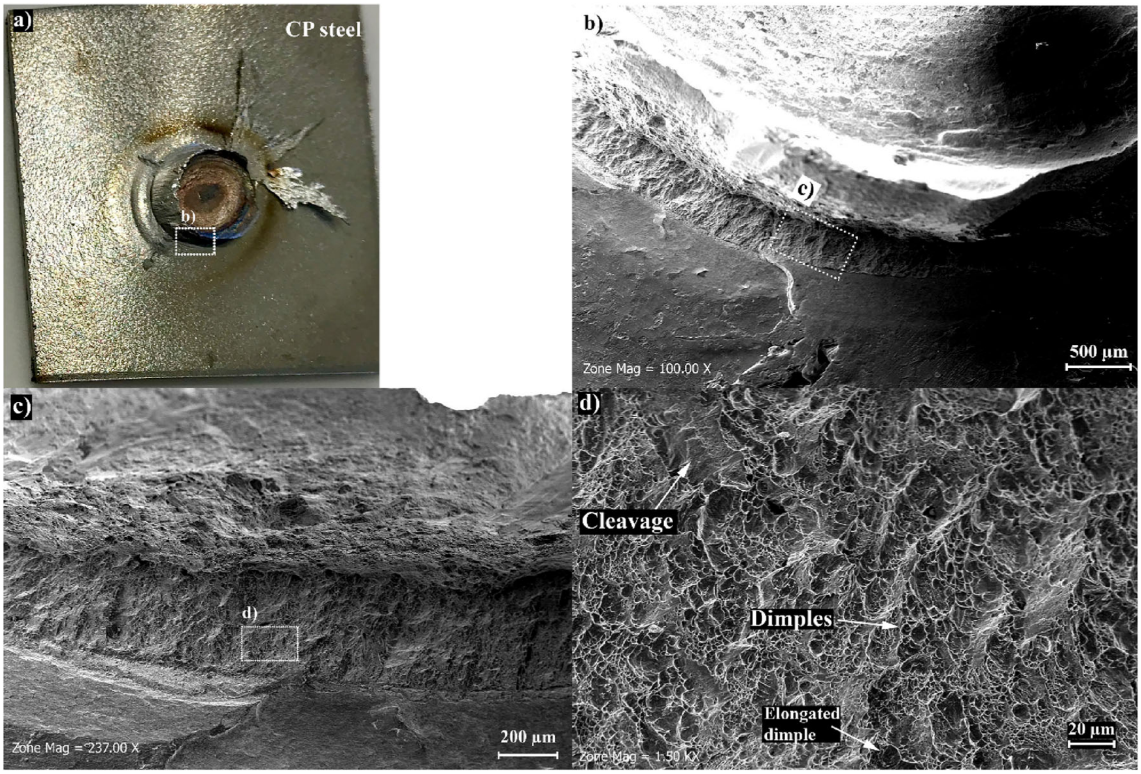

Figure 11. Fracture surface of CP800/DP1000HF with magnification of **a**) 2x, **b**) 100x, **c**) 237x and **d**) 1500x.

than that of CP800 steel. The sudden hardness change between the SCHAZ/ICHAZ zones caused the notch effect. This softening was less common in CP800 steel.

It was reported that the decrease in hardness of SCHAZ induces local plastic strains. The combined effect of dramatic hardness changes, local plastic strains and softening at the SCHAZ promoted the ruptures from DP1000HF steel. Premature the necking of the DP steels was also reported by various researchers [29, 32, 35, 39–41].

3.2 *Tensile-shear loads*

Tensile-shear tests are important for assessing load bearing performance of RSW applied weld joints. Figure 12 shows the tensile-shear bearing capacity in terms of welding time and welding currents. The weld nugget was not formed up to 8.2 kA and 6.9 kA welding currents for 5 and 10 cycle welding time, respectively. On the other hand, the weld joints over the 13.5 kA for 20 cycle, 11.9 kA for 25 and 30 cycle were overcurrent because high heat input fails to produce a weld nugget. The weld joint was drilled caused by full expulsion of the melted material because of the high heat input induced by elevated welding currents and welding durations. The maximum tensile shear load was obtained at 25 cycle welding time and 9.44 kA welding current as 26380 N. The lowest tensile-shear load was detected as 12702 N at the lowest heat input where 5 cycle welding time and 8.4 kA welding current was applied. The tensile-shear loads were increases up to a point then decreases because of expulsions and heat input relevant problems. The welding time of 5 cycle was an exception since the heat input to form sufficient nugget diameter was not enough.

The failure modes as well as the location of the failure are also significant because it describes the weakest region of the joint. The failure modes that encountered during tensile-shear tests were also embedded in the graph. Pull-out and interfacial fracture modes were observed. Figure 13 shows separation surfaces of the interfacial and pullout failure modes. All separations were fractured from the DP1000HF side because of softening at SCHAZ. CP800 was not affected from tensile-shear loads.

IF mode was encountered in only weld durations of 5, 10 and 15 cycle. The upper limit of the IF mode was 14 kA, 11 kA and 8.1 kA for 5, 10 and 15 cycle welding time, respectively. The rest of the welding durations was dominated by PF mode. This situation can be attributed to the elevated softening rate at HAZ of the DP1000HF steel induced by high heat inputs.

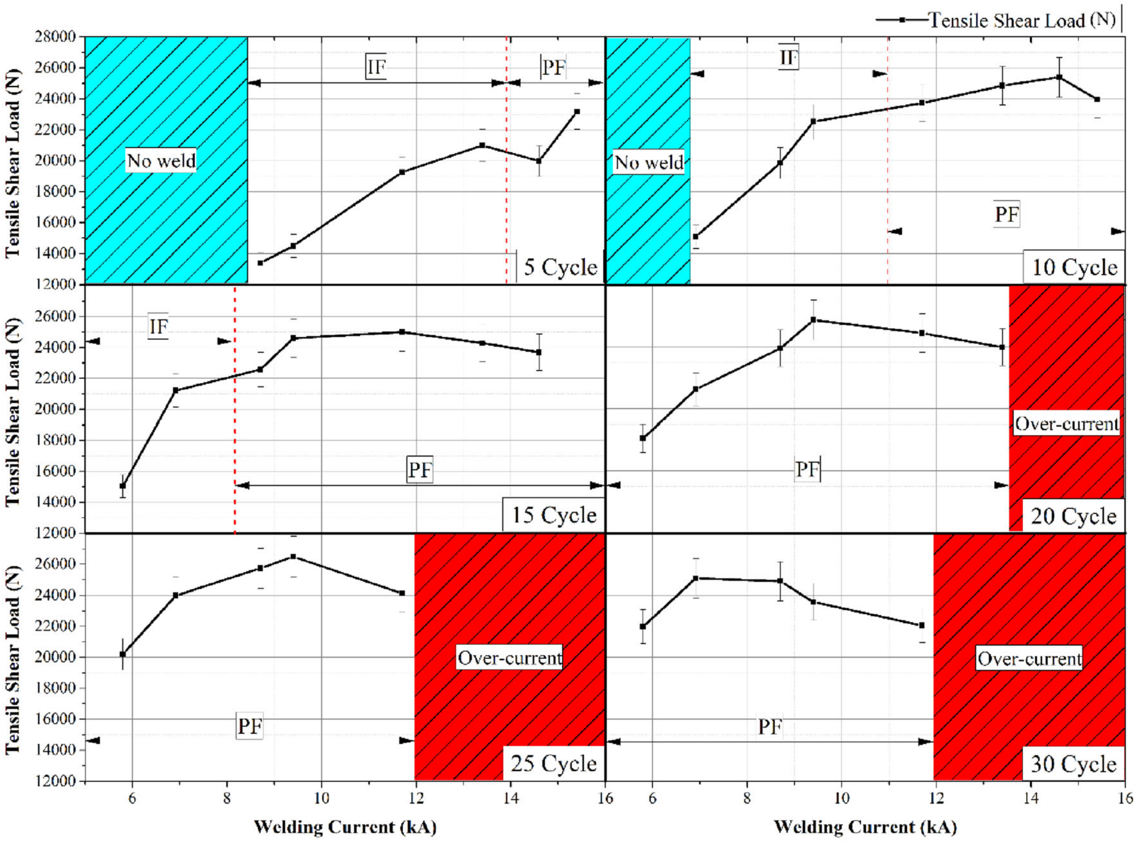

Figure 12. Tensile shear loads against welding currents and welding times.

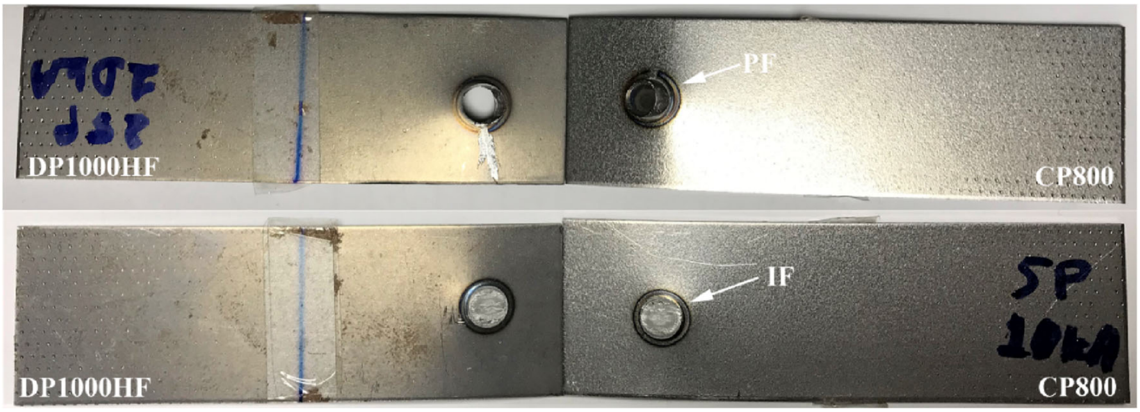

Figure 13. Failure modes of DP1000HF/CP800 joint obtained from tensile-shear tests.

3.3 *Weld nugget diameter*

Weld nugget diameter indicates the diameter of fusion zone that directly influences the tensile-shear load bearing capacity [42]. Figure 14 shows weld nugget diameter with tensile-shear load in terms of welding parameters. The curves obtained from the results were interpolated. The fracture modes were heavily influenced by the weld nugget diameter [43]. The maximum weld nugget diameter for IF fracture was observed as 7850 μm at 10 cycle welding time and 11 kA welding current where tensile-shear load was measured as 23830 N. On the other hand, the minimum weld nugget diameter produced from 5 cycle welding time 8.6 kA welding current was measured as 4050 μm. IF mode was generally obtained below the weld nugget diameter of 7500 μm that approximately corresponds to $6.3\sqrt{t}$. This transition line from IF to PF mode can be attributed to forming weld nugget diameter enough to bear tensile-shear load.

As heat input increased weld nugget diameter raised. This increasing trend was slowed down in high welding currents. Weld nugget diameter observed at the maximum tensile-shear load produced of 9.5 kA and 25 cycle welding time was measured as 9780 µm. The high heat input as a result of elevated welding current and welding time results in expulsions if weld nugget diameter exceeds the electrode force application diameter area [44]. The molten metal, which is under the pressure of the electrode force, ejects out of the weld nugget [45]. The molten metal ejected from the junction between two sheets. The ejected out some of the molten volume from the weld nugget is evenly squeezed by electrode application force decreasing height of the weld nugget and thickness of the HAZ. The severity of expulsion and reduced weld nugget height weakens the RSW applied joint. Therefore, the tensile-shear loads begin to decrease as the weld nugget diameter exceeds an optimum size.

3.4 *Electrode indentation depth*

Although the load carrying capacity of the RSW joints are of high important, electrode indentation depths (EID) causes a visual problem. It can also lead to premature failures due to excessive concentration of the stress [46]. Therefore, investigating the electrode indentation depths in terms of welding parameters is important to evaluate failure modes and deformations. Figure 15 shows effect of welding parameters on electrode indentation depths for both joint side against tensile-shear loads. The increase in welding current and welding time caused an increase in electrode indentation depths. The maximum electrode indentation depth was obtained in 12.5 kA welding current and 30 cycle welding durations as 1200 µm and 905 µm for DP1000HF and CP800, respectively. In other words, the maximum indentation depth was obtained in applied maximum heat input. The EID values for welding parameters of the maximum tensile-shear bearing capacity, where the welding parameters of 25 cycle welding time and 9.44 kA welding current was applied, are 805 µm and 708 µm for DP1000HF and CP800, respectively.

The increase in the heat input increases degree of softening at HAZ. As the severity of heat input increases higher expulsions are obtained. Another aspect is to hold the molten metal at the weld nugget zone. Namely, the electrode pressure circle determined by electrode force and electrode tip diameter act as a barrier to prevent expulsions. If else, the molten metal expulses from weld nugget and leads to elevated electrode indentation depths.

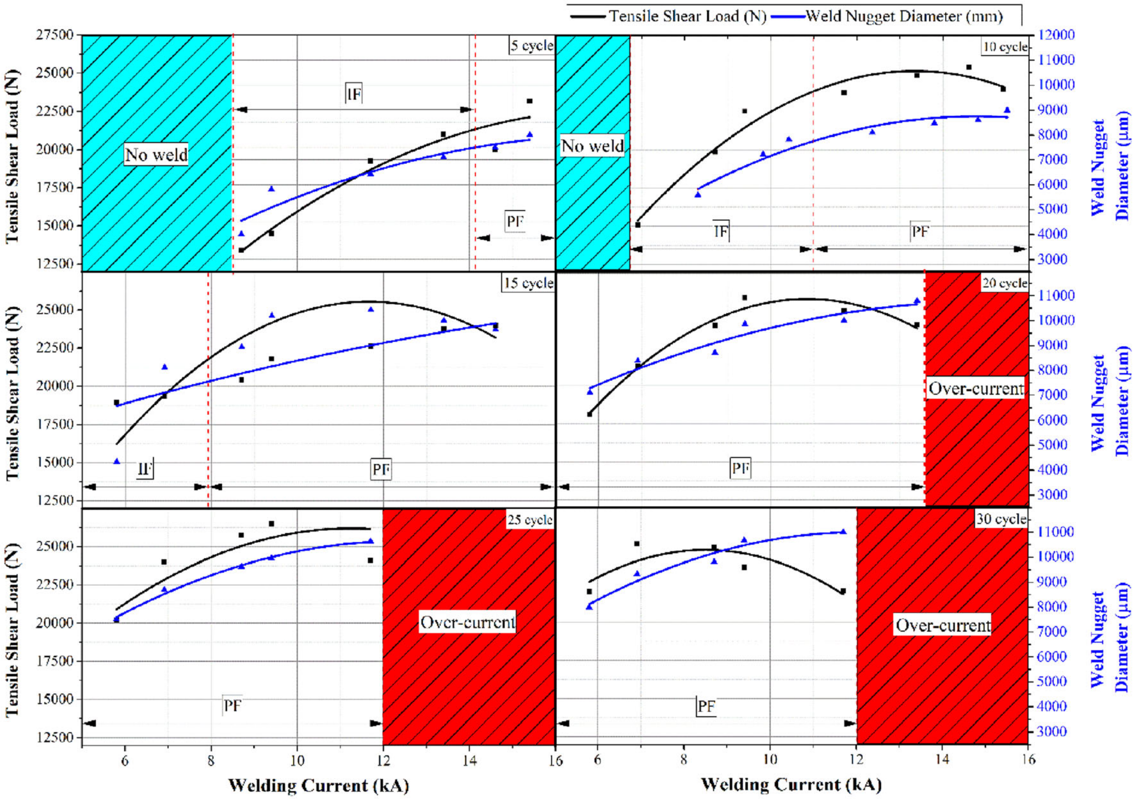

Figure 14. Obtained weld nugget diameters against tensile-shear loads in terms of welding currents and welding times.

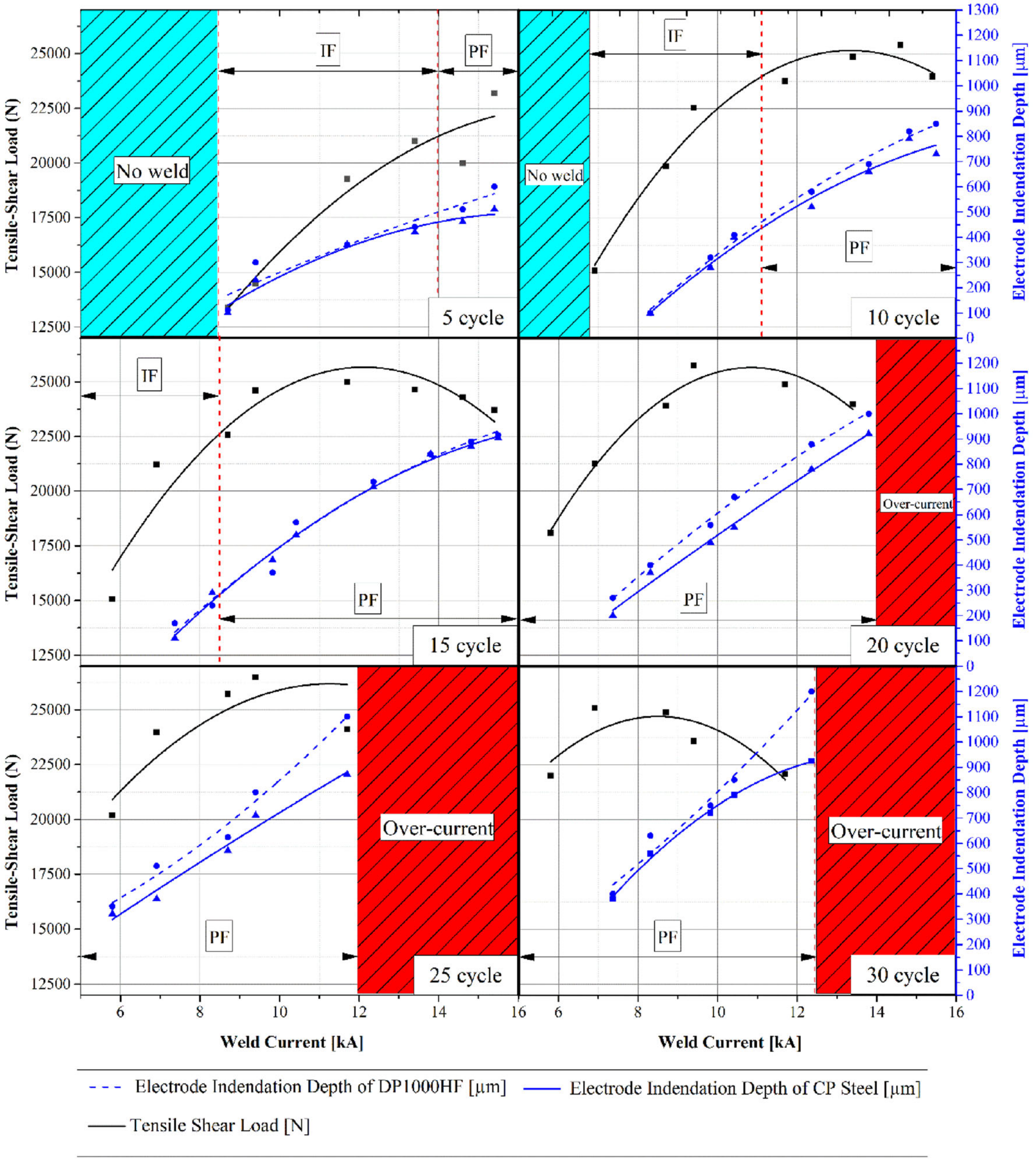

Figure 15. Electrode indentation depths of DP1000HF and CP800 against tensile-shear loads in terms of welding currents and welding times.

According to the results, heat input rate has linear effect on the EID of both sides. However, DP1000HF showed more EID than CP800 steel side. The divergence between DP1000HF and CP800 reaches to the maximum point at 30 cycle welding time and 12 kA welding current.

The main reason for different EID is the decreased high temperature strength, namely, early softening of the steel during RSW [47]. Chemical composition of DP1000HF steel yielded a low melting point and caused softening at elevated temperatures [48–50]. For these reasons, the DP1000HF exhibited more EID than CP800 steel.

3.5 *Weld lobe*

The weld lobe is a reference chart illustrating applicable welding parameters. Weld lobe is also an indicator of aesthetic appearance versus tensile-shear bearing capacity. Weld lobe is determined in the light of tensile-shear loads, failure types and electrode indentation depths. The determining criteria for tensile-shear loads was from 80% to 100% of the maximum tensile-shear load. Since IF failure implies that the weakest region is the weld nugget zone, IF was not included in calculation of the weld lobe. Electrode indentation depths below 30% of total sheet thickness was

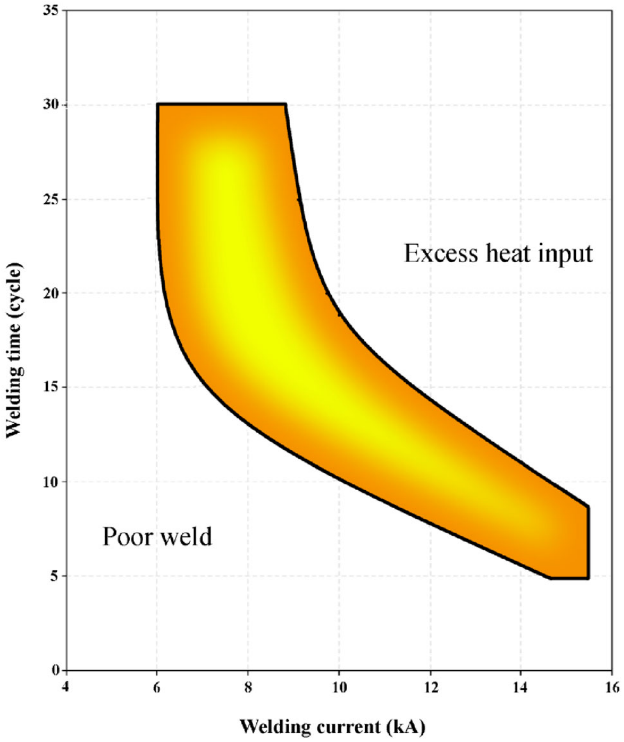

Figure 16. Weld lobe of RSW applied DP1000HF/CP800 joint.

regarded as acceptable welding parameters as described in AWS D8.7 standard. The sum of all accepted parameters were gathered and plotted. To complement the boundary of the weld lobe curve, some minimal predictions were also included to graph.

Weld lobe curve of RSW applied DP1000HF/CP800 joint is shown in Figure 16. According to weld lobe, acceptable weld limits are between 6 and 8.5 kA for 20, 25 and 30 cycle welding durations. Below 20 cycle welding times, the applicable welding currents were extended to 15.8 kA welding currents. In region of excess heat input, the indentation depths were increased. Tensile-shear loads were also elevated at a definite point. Conversely, the poor weld region where the lowest heat inputs were applied describes formation of insufficient weld nugget and tensile-shear load capacity. Since the applied heat inputs were weak, the electrode indentation depths were also low that increases aesthetic appearance.

The yellow region inside the weld lobe curve indicates the best results. As move to red areas towards excess heat input region, tensile-shear bearing capacity of the joint and electrode indentation depths increases. As moved to converse direction from the yellow areas, electrode indentation depths decrease that yields high aesthetic appearance, but tensile-shear bearing capacity decreases. It should be noted that the weldability ranges are valid only under 4 kN electrode force since electrode force increases the indentation depths.

4. Conclusions

Resistance spot welding of dissimilar DP1000HF/CP800 joints was successfully performed. Influence of different welding currents and welding time on tensile-shear load bearing capacity, weld nugget diameter and electrode indentation depths has been investigated. Their microstructures have been characterized by optical microscope, SEM and SEM/EBSD devices. In the light of results obtained, following major findings can be summarized as below;

- The maximum tensile shear load was obtained as 26380 N at 25 cycle welding time and 9.44 kA welding current. The maximum tensile-shear load for IF failed specimens was 22480 N at 10 cycle welding time and 11 kA welding current.
- While weld nugget diameter the maximum tensile-shear load among the IF failed specimens was measured as 7850 μm, weld nugget diameter at the maximum-tensile shear load was measured as 9780 μm.
- IF failure modes were generally obtained below $6.3\sqrt{t}$ that corresponds to the weld nugget diameter of 7500 μm.
- The lowest harnesses were obtained SCHAZ of both steels. Hardness drop was resulted from tempering of martensite and bainite. Since severity of the hardness drop at SCHAZ of the CP800 was less than DP1000HF, the pullout separation modes were continuously failed from DP1000HF side.
- The SCHAZ of both sides have exhibited a decrease in hardness. Hardness drops in SCHAZ with respect to BM was 8.04% for CP800 and 17.6% for DP1000HF.
- The softening in SCHAZ of DP1000HF compromised the weakest location of the joint except for IF separation modes. Therefore, tensile-shear bearing capacity have been limited by degree of softening in SCHAZ of DP1000HF.
- DP1000HF showed more EID than CP800 steel side due to early softening. The deviation of EID between DP1000HF and CP800 reaches to the maximum point at 30 cycle welding time and 12 kA welding duration.
- Fracture surface of the DP1000 mainly composed of dimples with rare cleavages that signifies characteristics of the ductile rupture.
- A narrow weld lobe curve was obtained because of the tensile-shear tests that failed with IF separation mode.

References

[1] Al-Abri O S, Pervez T, Qamar S Z and Khan R 2016 On the performance analysis of AHSS with an application to SET technology - FEM simulations and experimental measurements. *Thin-Walled Struct.* 101: 58–74

[2] Rossini M, Spena P R, Cortese L, Matteis P and Firrao D 2015 Investigation on dissimilar laser welding of advanced high strength steel sheets for the automotive industry. *Mater. Sci. Eng. A* 628: 288–296

[3] Lun N, Saha D C, Macwan A, Pan H, Wang L, Goodwin F and Zhou Y 2017 Microstructure and mechanical properties of fibre laser welded medium manganese TRIP steel. *Mater. Des.* 131: 450–459

[4] Di H S, Sun Q, Nie X K, Wang X N and Chen X M 2017 Mirostructure and properties of laser welded joints of dual phase and press-hardened steels. *Procedia Eng.* 207: 1665–1670

[5] Hudgins A W and Matlock D K 2016 The effects of property differences in multiphase sheet steels on local formability. *Mater. Sci. Eng. A* 654: 169–176

[6] Robl T, Krempaszky C, Fillafer A and Werner E 2021 Examining the unloading behavior of dual-phase steels by means of microstructure simulations. *Mater. Sci. Eng. A* 823(3): 1–9

[7] Wu Y, Uusitalo J and DeArdo A J 2021 Investigation of the critical factors controlling sheared edge stretching of ultra-high strength dual-phase steels. *Mater. Sci. Eng. A* 828: 1–12

[8] Roodgari M R, Jamaati R and Jamshidi Aval H 2021 A new method to produce dual-phase steel. *Mater. Sci. Eng. A* 803(12): 1–14

[9] Wang J, Li W, Zhu X and Zhang L 2022 Effect of martensite morphology and volume fraction on the low-temperature impact toughness of dual-phase steels. *Mater. Sci. Eng. A* 832: 1–10

[10] Mostaan H, Saeedpour P, Ahmadi H and Nouri A 2021 Laser welding of dual-phase steels with different silicon contents: Phase evolutions, microstructural observations, mechanical properties, and fracture behavior. *Mater. Sci. Eng. A* 811(9): 1–12

[11] Pramanick A K, Das H, Lee J W, Jung Y, Cho H H, Hong S T, Shome M and Pramanick A K 2021 Texture analysis and joint performance of laser-welded similar and dissimilar dual-phase and complex-phase ultra-high-strength steels. *Mater. Charact.* 174: 1–11

[12] Xu S S, Lu X H, Liu S C, Chen L, Zhang Y, Li X Z and Zhang Z W 2021 Precipitation strengthening of Cu/NiAl co-precipitates in a martensite-austenite dual-phase steel. *Mater. Charact.* 182: 1–7

[13] Sweet G A W, Donaldson I W, Schade C T, Amegadzie M Y and Bishop D P 2021 Laser free-form fabrication of dual phase DP600 steel using water atomized feedstock powder. *Addit. Manuf.* 47: 1–16

[14] Tu X, Shi X, Yan W, Li C, Shi Q, Shan Y and Yang K 2022 Tensile deformation behavior of ferrite-bainite dual-phase pipeline steel. *Mater. Sci. Eng. A* 831: 1–16

[15] Chen H, Lv Z, Lu L, Huang Y and Li X 2021 Correlation of micro-galvanic corrosion behavior with corrosion rate in the initial corrosion process of dual phase steel. *J. Mater. Res. Technol.* 15: 3310–3320

[16] Espinosa E, Sardar A, Simha C H M and Bardelcik A 2021 Realistic morphology-based Representative Volume Elements for dual-phase steels. *Mech. Mater.* 160: 1–9

[17] Kong J P, Han T K, Chin K G, Park B G and Kang C Y 2014 Effect of boron content and welding current on the mechanical properties of electrical resistance spot welds in complex-phase steels. *Mater. Des.* 54: 598–609

[18] Chang Y, Lin M, Hangen U, Richter S, Haase C and Bleck W 2021 Revealing the relation between microstructural heterogeneities and local mechanical properties of complex-phase steel by correlative electron microscopy and nanoindentation characterization. *Mater. Des.* 203: 1–11

[19] Martin P, Unruh K, Chottin J and Hug E 2018 Damage mechanisms in multiphased steels with a bainitic matrix under various mechanical loading paths. *Procedia Manuf.* 15: 1557–1564

[20] Sun H, Wei K, Yang X, Xiao Z and Wu Y 2020 Effects of pre-strain and annealing on the fatigue properties of complex phase steel CP800. *Int. J. Fatigue* 131: 1–11

[21] Lee H B, Lee H H, Song Y B, Ham J, Kim Y J, Kim H K and Suh D W 2021 Influence of chronological control of transformation on the microstructure and mechanical properties of complex phase steels. *Scr. Mater.* 200: 1–6

[22] Kumar R and Singh N K 2020 Modelling and simulation on behaviours of high strength steels. *Mater. Today Proc.* 28: 2345–2352

[23] Suppan C, Hebesberger T, Pichler A, Rehrl J and Kolednik O 2018 On the microstructure control of the bendability of advanced high strength steels. *Mater. Sci. Eng. A* 735: 89–98

[24] Das H, Mondal M, Hong S T, Lim Y and Lee K J 2018 Comparison of microstructural and mechanical properties of friction stir spot welded ultra-high strength dual phase and complex phase steels *Mater. Charact.* 139: 428–436

[25] Rajarajan C, Sivaraj P, Seeman M and Balasubramanian V 2020 Influence of electrode force on metallurgical studies and mechanical properties of resistance spot welded dual phase (DP800) steel joints. *Mater. Today Proc.* 22: 614–618

[26] Khodabakhshi F, Kazeminezhad M and Kokabi A H 2012 Resistance spot welding of ultra-fine grained steel sheets produced by constrained groove pressing: Optimization and characterization. *Mater. Charact.* 69: 71–83

[27] Özsaraç U, Onar V, Özen F, Aslanlar Y S and Akkaş N 2019 Effect of current and welding time on tensile-peel strength of resistance spot welded TWIP 1000 and martensitic steels. *Indian J. Chem. Technol.* 26: 248–251

[28] Xue X, Pereira A B, Amorim J and Liao J 2017 Effects of pulsed Nd: YAG laser welding parameters on penetration and microstructure characterization of a DP1000 steel butt joint. *Metals (Basel).* 7: 2–18

[29] Chabok A, Van der A E, De Hosson J T M and Pei Y T 2017 Mechanical behavior and failure mechanism of resistance spot welded DP1000 dual phase steel. *Mater. Des.* 124: 171–182

[30] Zhang M, Li Q, Huang C, Wu R, Fu R, Li L and Fang P 2013 Weldability of Ti-microalloyed Advanced High Strength Steel CP 800. *Adv. Mater. Res.* 634–638: 2899–2903

[31] Chen T, Ling Z, Wang M and Kong L 2020 Effect of a slightly concave electrode on resistance spot welding of Q&P1180 steel. *J. Mater. Process. Technol.* 285: 1–10

[32] Kundu J, Ray T, Kundu A and Shome M 2019 Effect of the laser power on the mechanical performance of the laser spot welds in dual phase steels. *J. Mater. Process. Technol.* 267: 114–123

[33] Xia M, Biro E, Tian Z and Zhou Y N 2008 Effects of heat input and martensite on HAZ softening in laser welding of dual phase steels. *ISIJ Int.* 48: 809–814

[34] Wang J, Yang L, Sun M, Liu T and Li H 2016 Effect of energy input on the microstructure and properties of butt joints in DP1000 steel laser welding. *Mater. Des.* 90: 642–649

[35] Chabok A, Van der A E and Pei Y 2020 A study on the effect of chemical composition on the microstructural characteristics and mechanical performance of DP1000 resistance spot welds. *Mater. Sci. Eng. A* 788: 139501

[36] Bandyopadhyay K, Panda S K and Saha P 2014 Investigations into the influence of weld zone on formability of fiber laser-welded advanced high strength steel. *J. Mater. Eng. Perform.* 23: 1465–1479

[37] Bao L, Wang Y and Han T 2021 Study on microstructure-toughness relationship in heat affected zone of EQ70 steel by laser-arc hybrid welding. *Mater. Charact.* 171: 110788

[38] Morawiec M, Różański M, Grajcar A and Stano S 2017 Effect of dual beam laser welding on microstructure–property relationships of hot-rolled complex phase steel sheets. *Arch. Civ. Mech. Eng.* 17: 145–153

[39] Bayock F N, Kah P, Salminen A, Belinga M and Yang X 2020 Feasibility study of welding dissimilar Advanced and Ultra High Strength Steels. *Rev. Adv. Mater. Sci.* 59: 54–66

[40] Angelastro A, Casalino G, Perulli P and Russo P 2018 Weldability of TWIP and DP steel dissimilar joint by laser arc hybrid welding with austenitic. *filler* 67: 607–611

[41] Pandre S, Mhatre V, Kotkunde N and Kumar S 2021 Materials Today: Proceedings Strain hardening behavior of DP 590 steel using dislocation density based Kock-Mecking model. *Mater. Today Proc.* 46: 9323–9327

[42] Vijayan V, Murugan S P, Son S G and Park Y D 2019 Shrinkage Void Formation in Resistance Spot Welds: Its Effect on Advanced High-Strength-Steel Weld Strength and Failure Modes. *J. Mater. Eng. Perform.* 28: 7514–7526

[43] Wei S T, Liu R D, Lv D, Lin L, Xu R J, Guo J Y, Wang K Q and Lu X F 2015 Weldability and mechanical properties of similar and dissimilar resistance spot welds of three-layer advanced high strength steels. *Sci. Technol. Weld. Join.* 20: 20–26

[44] Özen F and Aslanlar S 2021 Mechanical and microstructural evaluation of resistance spot welded dissimilar TWIP/martensitic steel joints. *Int. J. Adv. Manuf. Technol.* 113: 3473–3489

[45] Vijayan V, Murugan S P, Ji C, Son S G and Park Y D 2021 Factors affecting shrinkage voids in advanced high strength steel (AHSS) resistance spot welds. *J. Mech. Sci. Technol.* 35: 1–6

[46] Lu Y, Peer A, Abke T, Kimchi M and Zhang W 2018 Subcritical heat affected zone softening in hot-stamped boron steel during resistance spot welding. *Mater. Des.* 155: 170–184

[47] Ling Z, Chen T, Wang M and Kong L 2020 Reducing liquid metal embrittlement cracking in resistance spot welding of Q&P980 steel. *Mater. Manuf. Process.* 35: 1392–1399

[48] Liu H, Liu J, Wu B, Shen Y, He Y, Ding H and Su X 2017 Effect of Mn and Al contents on hot ductility of high alloy Fe-xMn-C-yAl austenite TWIP steels. *Mater. Sci. Eng. A* 708: 360–374

[49] Hamada A S and Karjalainen L P 2011 Hot ductility behaviour of high-Mn TWIP steels. *Mater. Sci. Eng. A* 528: 1819–1827

[50] Iwasaki Y and Fukumoto S 2020 High-temperature embrittlement in si-added austenitic stainless steel. *ISIJ Int.* 60: 756–763